Origin of double-peak precipitation hardening in metallic alloys

Haidong Fan[1*], A.H.W. Ngan[2*], Kefu Gan[2], Jaafar A. El-Awady[3]

[1] Department of Mechanics, Sichuan University, Chengdu 610065, P. R. China

[2] Department of Mechanical Engineering, The University of Hong Kong, Hong Kong, P. R. China

[3] Department of Mechanical Engineering, Whiting School of Engineering, The Johns Hopkins University, Baltimore, MD 21218, USA

[*] Corresponding Authors E-mails: hfan85@scu.edu.cn (H. Fan), hwngan@hku.hk (A.H.W. Ngan)

Abstract

Whereas conventional precipitation hardening is well-known to feature a single hardness peak, recently, double-peak precipitation hardening was observed, where the first peak hardness is higher than the second conventional one, thus offering a new approach to strengthen materials. Yet, classical precipitation strengthening models fail to predict such high strengthening in the early aging stage. In this work, molecular dynamics simulations were firstly performed to obtain a realistic dislocation-precipitate interaction law at the nano-scale, which was introduced into the discrete dislocation dynamics (DDD) method so as to investigate the precipitation hardening effects at the micro-scale. The DDD simulations correctly predict the double-peak hardening, namely, the critical resolved shear stress (CRSS) for a dislocation passing through a precipitate field first decreases, then increases, and finally decreases, as the precipitate radius r_p increases. Then, a precipitate shearing model was developed, which agrees well with the DDD simulations and experimental observations. Based on the DDD simulations and theoretical analysis, the three CRSS regimes were found to be controlled by coherency strengthening ($\mathrm{CRSS} \propto r_p^{-1/2}$), chemical strengthening ($\mathrm{CRSS} \propto -r_p^{-1}$) and Orowan mechanism ($\mathrm{CRSS} \propto r_p^{-1}$), respectively. Finally, a universal law for the inverse relation between the CRSS and precipitate size at the second, conventional peak was unveiled, while the first peak was found to occur favorably for rapid precipitation in the early aging stage. This work provides new insights into precipitation hardening in general and double-peak hardening in particular, which are of great importance for alloy design.

Keywords: double-peak precipitation hardening, discrete dislocation dynamics simulation, molecular dynamics simulation, precipitate shearing model, precipitation hardening mechanisms

1. Introduction

Metallic materials for structural applications are predominantly alloys, such as steels, aluminum alloys, titanium alloys, and superalloys. The mechanical properties of pure metals can be improved significantly by the addition of one or more alloying elements, i.e. precipitation strengthening (Ardell, 1985). In addition, precipitation or aging is also a flexible processing method with a wide application in industry. Therefore, it is of great significance to gain a complete understanding of the underlying mechanisms of precipitation hardening, as well as to construct physical models capable of predicting their effects on the mechanical properties of metallic alloys.

The conventional age or precipitation hardening curves exhibit a single hardness peak and two distinct hardening stages. In the first stage, an increasing hardness was observed with increasing aging time, and it was attributed to dislocations shearing precipitates, while the second stage beyond the hardness peak results from dislocations bypassing precipitates via the Orowan looping mechanism, leading to a decreasing hardness. Recently, a double-peak precipitation hardening was observed in aluminum alloys (Li et al., 2004; Yang et al., 2014; Zhao et al., 2013) and maraging steels (Pereloma et al., 2004; Shekhter et al., 2004), in which another peak in hardness occurs before the conventional peak, and, interestingly, the first hardness peak can even be higher than the conventional one (Li et al., 2004). The first hardness peak was attributed to profuse co-clusters having 1-2 nanometer thickness, such as Guinier–Preston (GP) zones in aluminum alloys and Ni-Ti clusters in maraging steels, while the second peak is due to metastable particles. Surprisingly, the addition of Cd or Sn in Al-Si alloys was observed to eliminate the second conventional hardness peak, so only the first peak prevails (Runxia et al., 2010). Since 1961, double-peak precipitation hardening was observed in many studies (Cook and Nutting, 1969; Kaçar and Güleryüz, 2015; Mimica, 2015; Nicholson and Nutting, 1961; Silva et al., 2014; Tan and Said, 2009) although it was overlooked. Despite the existence of only one global hardness peak in most alloys, for example typically the classical Al-Cu alloys by Ashby et al. (Ashby and Jones, 2013), a local plateau induced by rapid hardening was always observed before the global peak (Ralston et al., 2010), which was also attributed to the presence of nano-co-clusters (Starink and Wang, 2009; Xu et al., 2010a; Xu et al., 2010b). It is seen that the strong strengthening effect of the nano-co-clusters in the early aging stage is probably a universal mechanism in all metallic alloys. Since the first hardness peak can be higher than the second conventional peak, double-peak precipitation hardening could be suitably exploited to offer a new approach to strengthen metallic alloys. However, so far, a mechanistic understanding of the double-peak precipitation

hardening phenomenon is far from complete, because the classical coherency strengthening model suggests a negligible strengthening effect of such nano-co-clusters (Ardell, 1985; Argon, 2007). Thus, there is a pressing need for a fundamental understanding of the co-cluster strengthening that is responsible for the double-peak precipitation hardening phenomenon.

In a more general context, although age hardening has been studied thoroughly, it is still of importance to explore precipitation hardening mechanisms for modern materials, such as magnesium alloys. Recently, driven by the engineering demand of structural weight reduction, magnesium alloys receive a lot of attention for potential use in automotive, aerospace and defense applications (Luo, 2013). However, in magnesium alloys, the precipitation hardening is not as significant as in aluminum alloys. In AZ91 (Mg-9Al-1Zn), second-phase precipitates of 15% volume fraction lead to an strength increase of G/15 (G is the shear modulus), whereas in 7075 aluminum alloy with 5% precipitates, the strength is improved by 0.3G (Hutchinson et al., 2005). The much weaker precipitation hardening in magnesium alloys is thought to be due to various precipitates with different shapes, and various dislocation characters, as well as the operation of deformation twinning (Fan et al., 2018). The current double-peak precipitation hardening could provide an alternative method to strengthen magnesium alloys.

As is well-known, precipitation hardening is mainly realized by the resistance of precipitates on dislocation motion. As such, discrete dislocation dynamics (DDD) simulations (Arsenlis et al., 2007; Benzerga et al., 2004; Ghoniem et al., 2000; Kubin et al., 1992; Liu et al., 2009; Van der Giessen and Needleman, 1995; Zbib and Diaz de la Rubia, 2002) can be an effective tool to study precipitation hardening. In the DDD method, dislocations are coarse-grained as discrete lines, where a number of physical dislocation mechanisms are taken into account, i.e. dislocation multiplication, long-range interaction, annihilation, dislocation glide, cross-slip, junction as well as jogs. In the past two decades, DDD was extensively employed to study various aspects of dislocation mediated plasticity, such as dislocation behaviors (El-Awady, 2015; Gao et al., 2011; Liu et al., 2017), grain boundaries (Fan et al., 2015a), precipitates (Záležák et al., 2017; Zhang and Ngan, 2018), twin boundaries (Fan et al., 2015b) as well as crack (Huang et al., 2014). In 2003, three dimensional (3D) DDD was firstly used to study dislocation–precipitate interactions, but the precipitates were simplified to be impenetrable to dislocations (Shin et al., 2003). Then, Huang et al. proposed a penetrable γ/γ’ interface model in 3D-DDD to explore the shearing of precipitates by dislocations in superalloys (Huang et al., 2012). Takahashi and Ghoniem introduced an elastic stress field around a coherent precipitate into DDD method and studied the size effects of precipitates

(Takahashi and Ghoniem, 2008). Recently, Lehtinen et al. employed a Gaussian function to model the interaction potential between dislocations and precipitates (Lehtinen et al., 2016), and showed that the critical stress increases with decreasing precipitate spacing. In the previous DDD work, however, they all failed to capture the double-peak precipitate hardening. This is because the realistic dislocation-precipitate interaction is really complex, as discussed below in the section of dislocation-precipitate interaction model. The previous precipitate models could describe some specific characters of precipitates, but cannot reflect the full characters of precipitates.

In order to address the aforementioned issues, molecular dynamics (MD) simulations were firstly performed to obtain a realistic dislocation-precipitate interaction law, which was introduced into DDD method to study the interactions between dislocations and a precipitate field at multi-scales. The focus is on the precipitate size effects on the material strength to mimic the actual age-hardening process and especially the double-peak precipitation hardening. Based on the multi-scale simulation results, a physical model for the precipitate shearing is proposed, which shows good agreement with the DDD simulations and experimental observations. The reminder of this paper is organized as follows. The computational methods and models are introduced in Section 2. The main results are presented and discussed in Section 3. Finally, concluding remarks are made in Section 4.

2. Methods and models

2.1 DDD simulation setup

In order to obtain a fundamental understanding of precipitation hardening, a dislocation and an array of precipitates are introduced into a cubic simulation cell in DDD simulations, as shown in Fig. 1A. The precipitates have a uniform radius r_p and spacing l_p. Since edge dislocations usually have higher mobility than screw counterparts in FCC/BCC crystals and would therefore be the main carriers of plastic deformation, the simulated dislocation is of edge character (Ghoniem et al., 2000). Periodic boundary conditions are applied along the three directions. A pure shear stress is applied on the top and bottom surfaces to drive the dislocation towards the precipitates. To avoid loading rate effects on the dislocation-precipitate interactions as observed in (Lehtinen et al., 2016), a quasi-static loading scheme is employed. Firstly, an initial shear stress is applied, which is high enough to move the dislocation towards the precipitates, but not shear or bypass the precipitates. This configuration is then relaxed for 100000 steps, before the shear stress is intermittently

increased by 1 MPa/20000 steps. The 20000 relaxation steps were found to be long enough for a full relaxation during each stress increment. Once the dislocation bypasses or shears the precipitates, the instantaneous shear stress is defined as the critical resolved shear stress (CRSS).

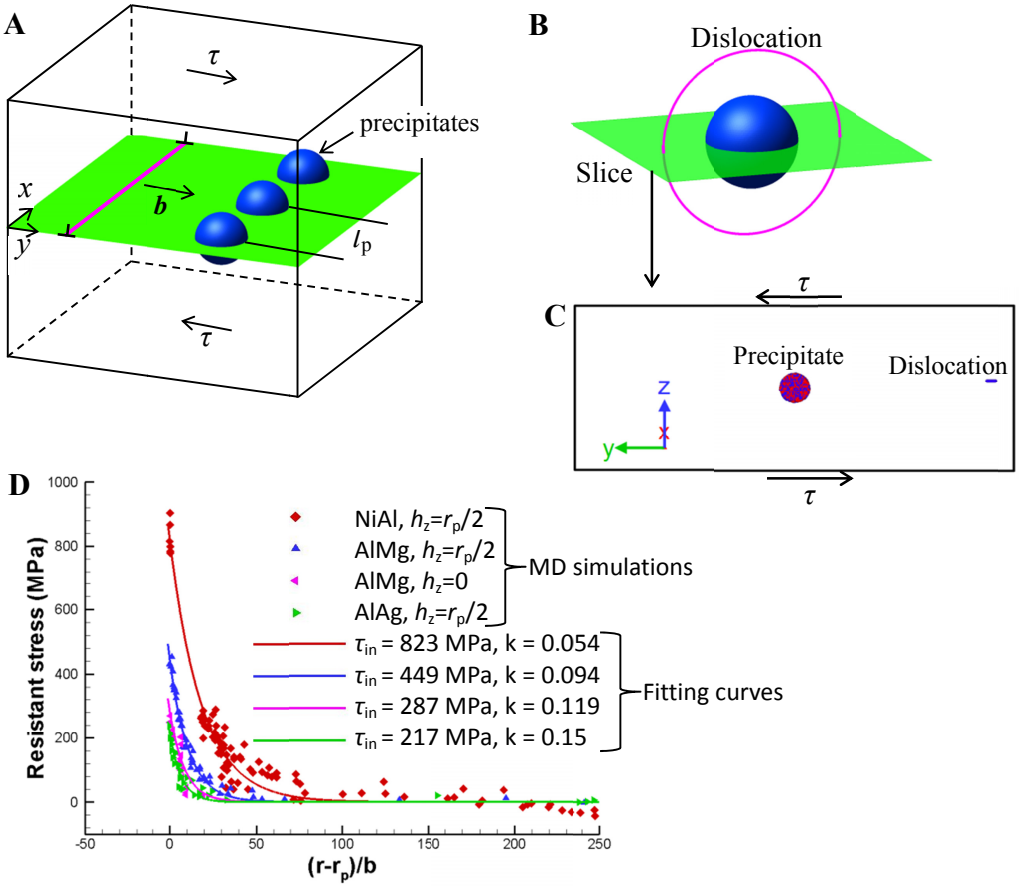

Fig. 1. Simulation cells used for DDD and MD simulations. (A) Schematic of the DDD simulation cell showing a dislocation and an array of spherical precipitates. The resistant stress on the dislocation is calculated in MD simulations, as shown in (B-D). (B) is a schematic of a spherical precipitate and a dislocation loop, which is an ideal configuration to calculate the resistant stress, but difficult to be realized in MD simulations. Instead, we make a slice with a disc precipitate and short dislocation, as shown in (C) from MD simulations. The resistant stress field as computed in MD simulations is shown in (D) as a function of the distance between the dislocation and precipitate interface.

All the DDD simulations were performed using the open source software, ParaDiS, developed in Lawrence Livermore National Laboratory (Arsenlis et al., 2007). In the ParaDiS, dislocations are treated as line defects, which are discretized into dislocation line segments. Under the external applied loading, $\boldsymbol{\sigma}_{\mathrm{ex}}$, all dislocation line segments considered in the simulation cell sense a total force per unit length equal to

$$\boldsymbol{F} = \boldsymbol{b} \cdot \left(\boldsymbol{\sigma}_{\mathrm{ex}} + \boldsymbol{\sigma}_{\mathrm{dis}} + \boldsymbol{\sigma}_{\mathrm{p}}\right) \times \boldsymbol{\xi} + \boldsymbol{F}_0 + \boldsymbol{F}_{\mathrm{self}} \tag{1}$$

where $\boldsymbol{b}$ is the Burgers vector of the dislocation segments, $\boldsymbol{\xi}$ is the dislocation line direction, $\boldsymbol{\sigma}_{\mathrm{dis}}$ is the long-range interaction stress between the current dislocation and others in the system, $\boldsymbol{\sigma}_{\mathrm{p}}$ is the resistant stress from precipitates, $\boldsymbol{F}_{\mathrm{self}}$ is the dislocation self-force, and $\boldsymbol{F}_0$ is the lattice friction force. Under this total force, each dislocation line segment glides with a velocity calculated using a linear mobility law

$$\boldsymbol{v} = \boldsymbol{F}/B \tag{2}$$

in which B is a drag coefficient. During dislocation glide, short-range dislocation interactions are taken into account, including cross-slip, junction and jog formation, annihilation as well as multiplication. In recent years, ParaDiS was employed frequently to model crystal plasticity in various situations, such as micropillars (Hussein et al., 2015), grain boundary strengthening (Fan et al., 2011), precipitation hardening (Lehtinen et al., 2016), deformation twinning (Fan et al., 2016), and so on.

2.2 Dislocation-precipitate interaction model

In ParaDiS, while various mutual interactions between dislocations were considered thoroughly, the interactions of dislocations with precipitates were not fully accounted for. Although several DDD studies were conducted to realize the precipitate shearing by dislocations (Huang et al., 2012; Lehtinen et al., 2016; Takahashi and Ghoniem, 2008), the double-peak precipitate hardening was not captured due to the lack of consideration of the full characters of precipitates. Therefore, a physical dislocation-precipitate interaction model is crucial for the current predictions of precipitation hardening.

Since the discovery of age hardening a century ago by Wilm (Wilm, 1911), much attention was directed towards understanding the precipitation hardening mechanisms. As reviewed by Argon (Argon, 2007) and Ardell (Ardell, 1985), various strengthening mechanisms were identified. These mechanisms can be grouped into two categories: hard-contact interactions and soft-contact interactions. The former includes chemical strengthening, stacking-fault strengthening and atomic-order strengthening. Chemical strengthening arises from the energy increase associated with the ledges on the precipitate-matrix interfaces sheared by dislocations. Stacking-fault strengthening originates from the energy change of the penetrating dislocations due to the stacking-fault energy difference between the precipitate and matrix. Atomic-order strengthening results from the energy consumption required for the formation of anti-phase boundaries (APB), which occur for ordered coherent precipitates, such as Ni_3Al in Ni-based superalloys. On the other hand, the soft-contact interactions include coherency strengthening and modulus misfit strengthening. Coherency strengthening is due to

the stress field sensed by the approaching dislocations around the coherent precipitates, as a result of the size misfit between the precipitate and matrix. Modulus misfit strengthening appears when the shear modulus of the precipitate differs from that of the matrix, which affects the line energy of the dislocation as it approaches the precipitate. In addition to the above-mentioned mechanisms, the misfit dislocation network formed on the precipitate-matrix interface could also produce a stress field near the interface and be a potential strengthening mechanism (Aaronson, 1974; Huang et al., 2012; Singh et al., 1988; Zhu et al., 2013).

The hard-contact interaction operates as short-range interactions between the precipitate interfaces and dislocations, where the interfaces are resistant to dislocations. Therefore, this resistance can be realized by an interface strength, τ_{in}. On the other hand, the soft-contact one produces hardening effects via a stress field around the precipitates. The resistant stress decays rapidly with the increasing distance from interface, but follows different mathematical functions for different strengthening mechanisms. The resistant stress from a coherent interface follows a power function (r^{-3}) (Argon, 2007), while that from a misfit dislocation network obeys an exponent function $\exp(-(r-r_{\mathrm{p}}))$ (Hirth and Lothe, 1982), where r is the distance from the precipitate center, and r_{p} is the precipitate radius. An explicit stress field from modulus misfit strengthening is unknown. Therefore, so far, a closed form function exactly describing the stress field around a precipitate is still unavailable.

To obtain a phenomenological stress field and introduce it into the DDD method, we performed molecular dynamics (MD) simulations to calculate the repulsive stress on a dislocation approaching a precipitate. This is a coarse-grain treatment, in which we do not need to consider specific interaction types. The MD simulation was performed using the open source "LAMMPS" code (Plimpton, 1995). Figure 1B is a schematic of a spherical precipitate and dislocation loop, which are an ideal configuration to calculate the resistant stress around a spherical precipitate, but difficult to be realized in MD simulations. Instead, we employed a slice in Fig. 1B, which is a simulation cell with a disc precipitate and short dislocation, as shown in Fig. 1C exported from MD simulations. The simulation cell has dimensions of X = 4.2 nm, Y = 160 nm and Z = 60 nm, and contains ~3.4 million atoms. Periodic boundary conditions are imposed in the X-Y plane, while free surface boundary conditions are imposed along the third direction. The periodic boundary conditions in the X-direction are able to eliminate the precipitate end effects on the dislocation-precipitate interactions. To have generality, three atomic potentials were used for three typical alloy systems, including Ni_3Al precipitate in Ni-Al alloys (Purja Pun and Mishin, 2009), Al_3Mg precipitate in Al-Mg alloys

(Liu and Adams, 1998) and Ag-rich precipitate in Al-Ag alloys (Zhou et al., 2004). In experiments, different precipitates were observed to have different atomic structures, such as $L1_2$ structure (He et al., 2016). However, in MD simulations, it is difficult to introduce the complex atomic structures, especially for the current disc precipitates with curved interfaces. Therefore, the precipitates are introduced by substituting the matrix atoms with the alloying atoms according to the precipitate component. All the precipitates are 8-10 nm in diameter. The dislocation is introduced by initializing all atoms according to the Volterra field (Fan et al., 2017). As is well-known, the precipitate has a different resistant stress on the dislocation when hit at a different position. Here the dislocation is placed in two positions by changing the dislocation vertical coordinate h_z with respect to the precipitate center. $h_z = 0$ when the dislocation hits the precipitate center, while $h_z = r_p/2$ when dislocation hits the hemisphere.

At the beginning of MD simulations, energy minimization is performed on the entire simulation cell to reach a zero-pressure state at temperature of 0 K. The dislocation is initially placed far away from the precipitate. A pure shear stress is then imposed on the free surfaces using NVE ensemble to drive the dislocation towards the precipitate. As is well-known, the loading rate in MD simulations is usually at the order of 10^8/s and cannot be used here to study the repulsive stress in equilibrium. So we employed a quasi-static loading scheme. We repeatedly increase the applied shear stress by an increment of 6.9 MPa in 20 ps (20000 steps) only when the dislocation reaches an equilibrium state (i.e. dislocation displacement is less than 1 nm in 20 ps). Such low loading rate was observed to introduce weak inertial effects (Fan et al., 2015c). The shear stress is applied continually until the dislocation shears the coherent precipitates. Under the quasi-static loading, the dislocation position can be easily monitored in MD simulations to calculate the dislocation distance from the precipitate interface.

In Fig. 1D, the resistant stress is shown as a function of the distance between the dislocation and precipitate surface. It is clear the resistant stress becomes strong as the dislocation is approaching the precipitate for the three alloy systems. To obtain a closed form function describing the resistant stress, then an exponential function is employed to fit the data, as follows,

$$\tau_{\mathrm{p}} = \tau_{\mathrm{in}} \exp(-k \frac{r - r_p}{b}) \tag{3}$$

which is shown to well match the stress field. τ_{in} is the interface strength, k represents the decay rate of the resistant stress, r is the distance from the precipitate center, r_{p} is the

precipitate radius, b is the magnitude of the Burgers vector. All the fitting parameters are shown in the legend of Fig. 1D.

From Fig. 1D and the fitting parameters, it is seen that the precipitation hardening effect is strong in NiAl alloys, and weak in AlAg alloys. This is mainly controlled by the size misfit between the matrix and precipitate, such as lattice constant is 40.5 Å for Al, 40.85 Å for Ag, 35.2 Å for Ni. In addition, the precipitate has a slightly strong resistant stress on the dislocation when the dislocation intersects its hemisphere. This is likely due to that the stress from coherency strengthening mechanism increases with increasing distance from the precipitate center (Argon, 2007). It should be noted that, although the introduced precipitate is fully coherent with the matrix, the stress field follows an exponent function for the three considered alloys rather than the field from coherency strengthening model (Askari et al., 2013). In addition, the coherency strengthening model suggests that the resistant stress should be zero at $h_z = 0$, while the resistant stress is considerable in MD simulations. We can see the stress field of coherent precipitates cannot be described by the coherency strengthening model any more (Askari et al., 2013). This is because in addition to the coherency strengthening mechanism, other strengthening mechanisms coexist there, such as chemical strengthening, stacking-fault strengthening and modulus misfit strengthening. As such the current MD simulations are more accurate than the stress field predicted analytically through any specific strengthening model.

Even though not all the strengthening mechanisms coexist in a given alloy, generally, there are at least one soft-contact and one hard-contact interactions between the dislocations and precipitates. Therefore, Eq. (3) should represent a general stress field applicable to any type of precipitates, while the particularity of the interface of one given precipitate type can be realized by adjusting the interface strength τ_{in} and stress decay rate k. Here, the interface strength τ_{in} controls the short-range interactions such as chemical strengthening, while k controls the strength of long-range interactions, such as the coherency strengthening. A smaller value of k yields a stronger coherency strengthening.

3. Results and Discussions

3.1 DDD simulations of precipitation hardening at constant precipitate volume-fraction

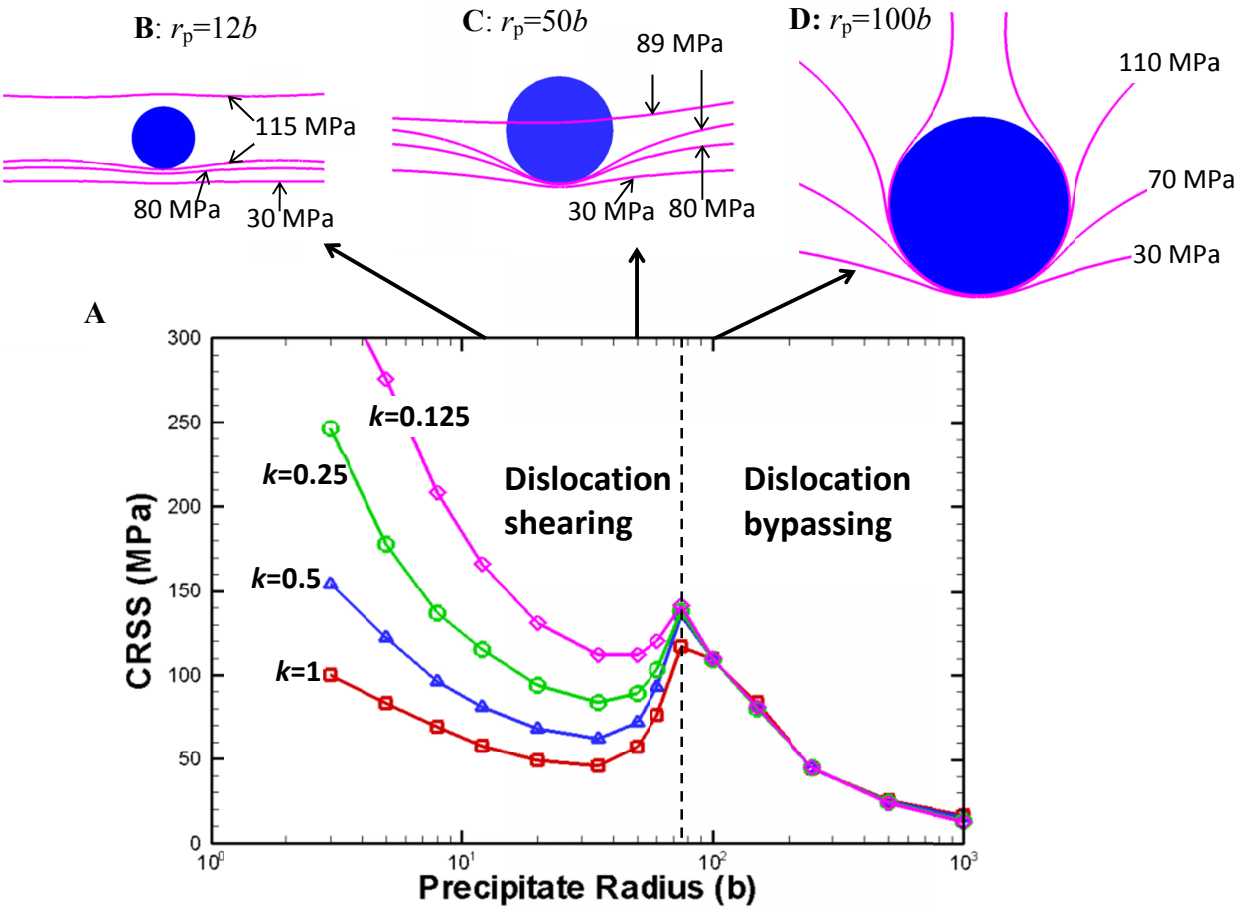

Fig. 2. DDD simulation results. (A) DDD computed CRSS as a function of the precipitate radius r_p and resistant stress decay rate k. Remaining figures are DDD simulations of the interactions between a dislocation and precipitates with radii (B) 12b, (C) 50b and (D) 100b, which are corresponding to the three regimes in (A). In each case, a sequence of snapshots at different applied shear stresses is shown.

In the DDD simulations, the following material properties were adopted to mimic the properties of aluminum alloys, in which precipitation strengthening is typical: shear modulus G = 26 GPa; Poisson ratio v = 0.33; and magnitude of the Burgers vector b = 0.25 *nm* (Hou et al., 2008). The drag coefficient, B, is set to be 1.6×10^{-3} Pa s, which is relatively high to stabilize the dislocation during the intermittent relaxation of quasi-static loading. The interface strength, τ_{in}, is 500 MPa. The precipitate volume fraction f_p is kept constant at 1%, which results in an average precipitate spacing of $l_p = \beta r_p$, where $\beta = \sqrt[3]{4\pi/3f_p} = 7.48$ is the precipitate spacing-to-radius ratio. Here, the precipitate radius was changed in the range of $r_p = 3b \sim 1000b$, and the decay rate k = [0.125, 0.25, 0.5, 1] to study their effects on the CRSS for a dislocation to shear or bypass an array of precipitates. During the aging process in experiments, the precipitate radius increases, accompanied by the changes in the precipitate volume fraction, precipitate spacing and interface strength.

To quantify the dependence of precipitation hardening on these variables, current simulations were carried out in iso-parametric conditions (i.e. quantifying the hardening effect as a function of precipitate radius by fixing the volume fraction, interface strength at specific values), while the influence of other parameters will be discussed in following sections. It should also be noted that in real alloys the precipitates may not have a sphere shape, especially for small coherent precipitates in the early aging stage. However, the dislocation-precipitate interaction mechanisms for spherical precipitates can provide the basis for predicting the interactions with plate-like or rod-like precipitates. A precipitation hardening model developed from DD simulations of spherical precipitates can thus be used to predict the hardening effects of other precipitates by introducing the geometrical information. Therefore, here we start with spherical precipitates.

The CRSS predicted from DDD simulations for different precipitate radii and stress decay rates is plotted in Fig. 2A. It is observed that the CRSS versus precipitate radius displays three regimes for any given stress decay rate. With the increasing precipitate radius, the CRSS firstly decreases, then increases, and finally decreases. In addition, the CRSS is observed to increase with the decreasing stress decay rate, and this is significant only for small precipitates ($r_p < 75b$). When the precipitate radius is larger than the critical value $r_p \sim 75b$, the stress decay rate has a negligible influence on the predicted CRSS, and all curves coincide. The distinct regimes observed on the CRSS-precipitate radius curves indicate that different dislocation mechanisms must be in effect. As shown in Figs. 2B-D, in the first two regimes, dislocation cutting the precipitates is the controlling mechanism, while dislocation bypasses the precipitates by the Orowan mechanism in the third regime. The CRSS at the transition from dislocation shearing to bypassing is typically referred to as the second precipitation hardening peak, which is observed to be weakly influenced by the stress decay rate. The latter two regimes agree well with previous observations, and have been studied extensively, whereas the first regime was not previously observed or predicted from simulations. In the first regime, the CRSS increases remarkably with decreasing precipitate radius. This is possibly indicative of the first precipitation hardening peak in the double-peak precipitation hardening observed in experiments (Li et al., 2004; Pereloma et al., 2004; Shekhter et al., 2004; Yang et al., 2014; Zhao et al., 2013). Moreover, the first regime is affected greatly by the stress decay rate. For a low stress decay rate (large coherency strain), the strengthening in the first regime is strong, and can even be higher than the second hardening peak, which agrees with experimental observations (Li et al., 2004). On the other hand, for a high stress decay rate and small

coherency strain, the stress in the first regime is low, indicating that the first hardening peak does not occur. This could explain why double-peak hardening was not commonly observed. It is worth noting that in Fig. 2A, the precipitate volume fraction is kept constant, thus, the CRSS is very high for small but profuse precipitates. In experiments, the precipitate volume fraction also changes as the precipitates grow during the aging process, and this will be considered in a latter section.

The interaction details between dislocations and precipitates are shown in Figs. 2B-D. The precipitates have radii of 12*b*, 50*b* and 100*b*, which are representative cases for the three regimes in Fig. 2A. In each case, a sequence of snapshots at different applied shear stresses is shown. In Fig. 2B, under a low stress of 30 MPa, the dislocation glides towards the precipitate and begins to sense the resistant stress field from the precipitate. At a shear stress of 80 MPa, the dislocation begins to bow between the precipitates. With increasing applied stress, the dislocation glides forward while meeting stronger resistant force from the precipitate, and finally, the dislocation touches the interface at a shear stress of 115 MPa. The dislocation segment then shears the interface and glides into the precipitate, cutting the whole precipitate. The interaction process for $r_p = 50b$ is similar to the case of $r_p = 12b$, as shown in Fig. 2C. The main difference is that the dislocation bows significantly between the precipitates due to the fact that the precipitate spacing also increases with increasing precipitate radius for a constant volume fraction.

For the case of $r_p = 100b$ shown in Fig. 2D, the dislocation bows and then loops around the precipitate, and at a shear stress of 70 MPa, it begins to wrap the precipitate. Further increase in the applied stress leads to further bowing of the dislocation, and at a shear stress of 110 MPa, the dislocation surrounds half of the precipitate interface. As is well-known, this is the critical configuration for bypassing, and the dislocation further wraps the precipitate and eventually pinch-off occurs without any further stress increase. This is in agreement with the Orowan mechanism, and finally a dislocation loop surrounding the precipitate is left.

3.2 Analytical precipitation hardening model based on precipitate shearing

While the DDD simulations in Fig. 2A successfully capture the dislocation shearing precipitates and predict the double-peak precipitation hardening, the detailed dependence of such important phenomena on material species would be better revealed by an analytical model. Since the Orowan bypassing mechanism has been studied thoroughly in

the past, the focus here will be on the case of dislocation shearing precipitates, which occurs in the first two regimes in Fig. 2A.

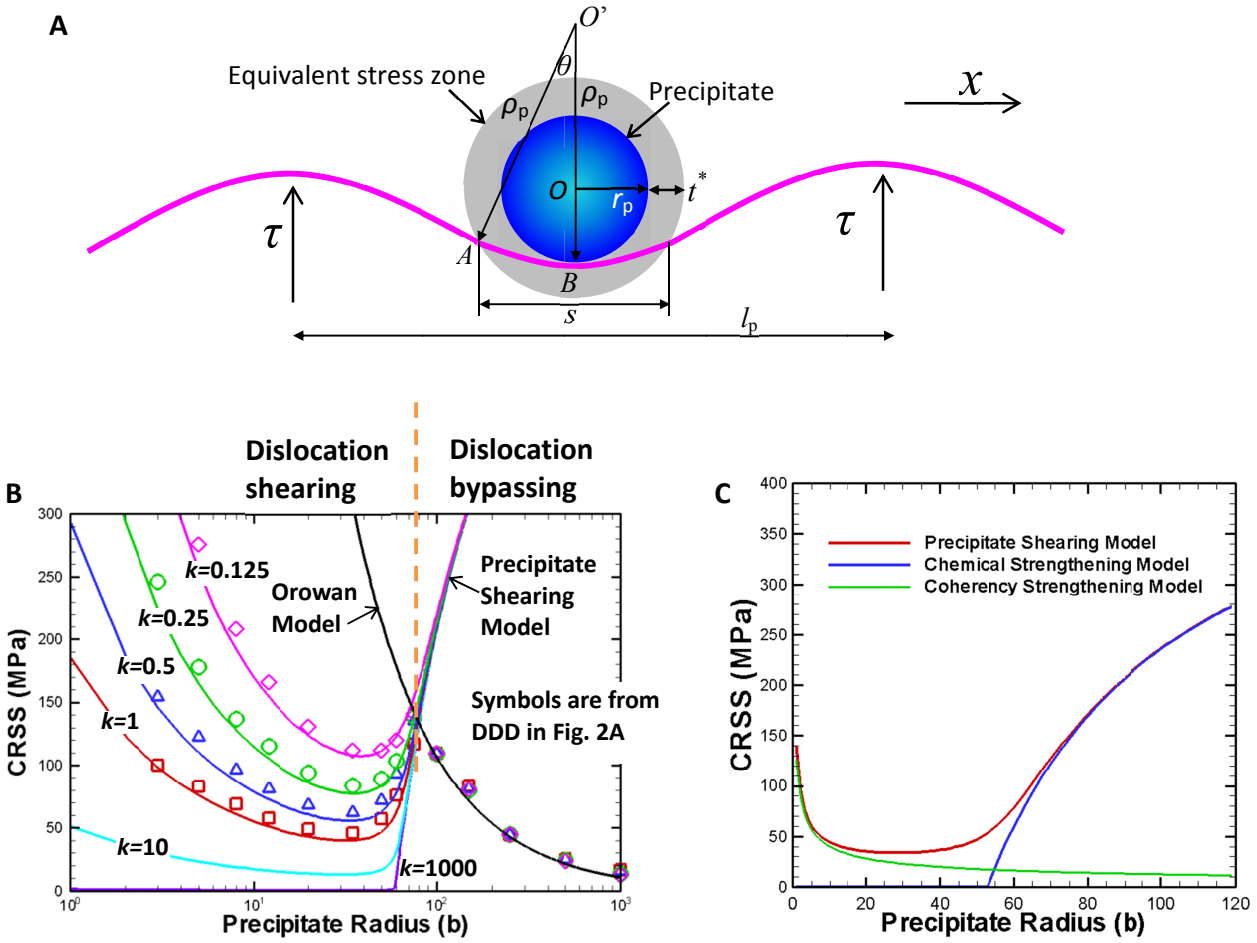

Fig. 3. Precipitate shearing model. (A) Schematic of the interaction between a dislocation and a precipitate at the critical moment the dislocation shears precipitate. (B) Comparison between the CRSS predicted from DDD simulations (discrete data symbols, from Fig. 2A) and the analytical precipitate shearing model and Orowan model (curves). (C) CRSS predicted by the precipitate shearing model, coherency strengthening model, and chemical strengthening model.

Table 1. Definition of the parameters used in the model.

Parameters	Symbol	Parameters	Symbol
Resistant stress field from the precipitate	τ_p	Applied shear stress	τ
Interface strength	τ_{in}	Decay rate of the resistant stress	k
Precipitate radius	r_p	Precipitate spacing	l_p
Thickness of the equivalent stress zone	t^*	Resistant stress in the equivalent stress zone	τ_p^*
Critical resolved shear stress	τ_{CRSS}	Span of the dislocation within the stress zone	s
Magnitude of the Burgers vector	b	Dislocation tension force	T
Radius of curvature of the dislocation	ρ	Radius of curvature of dislocation within the equivalent stress zone	ρ_p

For a dislocation approaching an array of precipitates, as shown in Fig. 1A and Fig. 3A, the dislocation experiences two forces due to the applied shear stress τ and the resistant stress field from the precipitates. Force equilibrium requires that

$$\int_{-l_p/2}^{l_p/2} \tau_p \, b dx = \int_{-l_p/2}^{l_p/2} \tau b \, dx = \tau b l_p \tag{4}$$

where τ is the applied stress, τ_p is the resistant stress field from the precipitate. Consideration of the line tension for any infinitesimal dislocation segment gives

$$\tau_p - \tau = \frac{T}{b\rho} \tag{5}$$

where T is the line tension force and ρ is the radius of curvature. Unfortunately, an analytical solution of the stress is unattainable because τ_p has a complex expression.

To obtain a closed form solution, the precipitate stress field τ_p is replaced by a constant equivalent stress $\tau_p^* = \tau_{in}$ that acts over an effective stress zone thickness t^* outside the precipitate, as shown in Fig. 3A. The thickness t^* is where $\tau_p = \tau_{in}/2$, which gives $t^* = \ln(2)b/k$. Eqs. (4) and (5) are then simplified significantly into

$$\tau_{in} s = \tau l_p \tag{6}$$

$$\tau_{in} - \tau = \frac{T}{b\rho_p} \tag{7}$$

where ρ_p is the radius of curvature of the dislocation within the stress zone, and s is the span of the dislocation within the stress zone, as shown in Fig. 3A. At the critical moment of the precipitate being sheared, the dislocation is able to penetrate the stress zone and touch the precipitate interface at point B. For a small precipitate, the dislocation bends slightly at precipitate, as shown in Fig. 2B, and

$$s \approx 2\,AB \tag{8}$$

According to the geometry for ΔAOB and ΔAO′B,

$$\cos(\angle ABO) = \frac{AB^2 + r_p^2 - (r_p + t^*)^2}{2 r_p AB} = \frac{AB}{2\rho_p} \tag{9}$$

Substituting the parameters ρ_p and AB in Eq. (9) with Eqs. (6-8) yields a final cubic equation

$$\tau^3 - M\tau^2 - N = 0 \tag{10}$$

where

$$M = \tau_{in} - \frac{T}{b r_p}; \quad N = 4\tau_{in}^2 \frac{T}{b r_p} \frac{t^*(t^* + 2r_p)}{l_p^2} \tag{11}$$

Solving Eq. (10), the CRSS is found to be

$$\tau_{\mathrm{CRSS}} = \frac{1}{3}\left(M + M^2 \sqrt[3]{\frac{2}{2M^3+27N+3\sqrt{12M^3N+81N^2}}} + \sqrt[3]{\frac{2M^3+27N+3\sqrt{12M^3N+81N^2}}{2}} \right) \quad (12)$$

which is the only positive real root of Eq. (10). Since the current model is associated with the dislocation shearing precipitates, it is referred to as precipitate shearing model. The definition of all the parameters is listed in Table 1.

A comparison between the current precipitate shearing model and DDD simulations is made in Fig. 3B. In addition, the Orowan model is shown as well,

$$\tau_{\mathrm{Orowan}} = \frac{2T}{b(l_{\mathrm{p}}-2r_{\mathrm{p}})} \quad (13)$$

We can see that dislocation shearing in the first two regimes is easier than dislocation bypassing, so precipitate shearing occurs. In the third regime, the Orowan model is lower than the precipitate shearing model, so dislocation bypassing occurs preferentially. As shown in Fig. 3B, the two models agree well with the DDD predictions of CRSS for all the stress decay rates considered.

In Fig. 3B, the CRSS for $k = 10$ and 1000 predicted from the precipitate shearing model is shown as well. It is observed that the CRSS curve of $k = 1000$ shows the second regime only, and is zero below a critical precipitate radius of $r_{\mathrm{p}} \sim 53b$. As discussed above, in Eq. (3) the interface strength τ_{in} controls hard-contact interactions (i.e. typically chemical strengthening), while k is related to soft-contact interactions, such as coherency strengthening for small precipitates. When $k = 1000$, the stress decays very fast and almost no coherency strengthening exists. So the chemical strengthening leads to the increasing CRSS with increasing precipitate radius, which is valid only in the second regime and agrees well with the previous observations (Ashby and Jones, 2013). Therefore, at the limit of $k \to \infty$, Eq. (12) becomes a model for chemical strengthening

$$\tau_{\mathrm{chem}} = \tau_{\mathrm{in}} - \frac{T}{br_{\mathrm{p}}} \quad (14)$$

Comparing between Eqs. (7) and (14), it is clear that the radius of curvature of the dislocation shearing the interface becomes the precipitate radius r_{p}, indicating that the dislocation always surrounds the precipitate interface. Therefore, this term T/br_{p} is the stress produced by dislocation line tension due to the curvature of dislocation, which helps the dislocation overcome the interface strength τ_{in}. However, with the decreasing precipitate radius, τ_{chem} becomes negative below a critical precipitate size of $T/(b\tau_{\mathrm{in}})$. This suggests that the dislocation is able to shear the interface of strength τ_{in} with the aid

of line tension force T/br_{p}, and thus τ_{chem} can be approximated as zero. In previous studies (Ardell, 1985), the chemical strengthening effect was claimed to be expressed by $\tau_{\mathrm{chem}} \propto r_{\mathrm{p}}^{-1}$, which, however, conflicts with the experimental observations. Thus, chemical strengthening was claimed to have a minor contribution to age hardening (Ardell, 1985). In contrast, here, the chemical strengthening effect shown in Eq. (14) affects significantly the second regime and second hardening peak, as discussed later.

Because the chemical strengthening effect dominates in the second regime only, the first regime mainly results from soft-contact interactions (i.e. coherency strengthening). With the decreasing decay rate k, the coherency strengthening becomes strong, and the first regime becomes remarkable. Therefore, it can be concluded that the first precipitation hardening peak observed in experiments is a result of strong coherency strengthening. Since coherency strengthening dominates for small precipitates, a simple coherency strengthening model can be derived. In Fig. 2B, the dislocation bends slightly when penetrating small precipitates. As a result, the dislocation can be simplified as a straight line, and according to Eq. (6),

$$\tau_{\mathrm{coh}} = 2\frac{\sqrt{2t^*r_{\mathrm{p}}+t^{*2}}}{l_{\mathrm{p}}}\tau_{\mathrm{in}} \approx 2\frac{\sqrt{2t^*r_{\mathrm{p}}}}{l_{\mathrm{p}}}\tau_{\mathrm{in}} = \frac{2\sqrt{2}}{\beta}\sqrt{\frac{t^*}{r_{\mathrm{p}}}}\tau_{\mathrm{in}} \qquad (15)$$

It is clear τ_{coh} is proportional to $r_{\mathrm{p}}^{-1/2}$, and increases with decreasing precipitate radius. It is worth noting that in previous studies the coherency strengthening model was represented by $\tau_{\mathrm{coh}} \propto r_{\mathrm{p}}^{1/2}$, and suggests a negligible hardening effect of small precipitates, which, however, exhibits a poor agreement with experiments (Ardell, 1985; Argon, 2007). Thus, the current model should provide new insights into the coherency strengthening effects.

A comparison between the precipitate shearing model (Eq. 12), the chemical strengthening model (Eq. 14) and the coherency strengthening model (Eq. 15), is made in Fig. 3C. For small precipitates with $r_{\mathrm{p}} < 20b$, the CRSS is dominated by coherency strengthening, while chemical strengthening dominates for large precipitates. As a result, the sum of Eqs. (14) and (15) would serve as a good approximation of the precipitate shearing model.

3.3 Prediction of double-peak hardening under realistic aging conditions

The above theoretical considerations show that, on increasing precipitate size at constant precipitate volume fraction, the alloy strength in general first exhibits a drop due

to precipitate shearing, followed by the conventional hardening peak corresponding to precipitate bypassing via the Orowan process. The occurrence of the initial strength drop is found to be an intricate result of the precipitate-matrix interfacial strength, the stress zones around the precipitates and their spacing, and the local curvature of the interacting dislocation. With now the basic mechanics of the double-peak hardening elucidated, we can proceed to predict realistic aging curves under experimental conditions. However, at this juncture, it is important to realize that the theoretical predictions above are based on the conditions of constant precipitate volume fraction and spherical precipitate shape, while in real, experimental aging conditions, both the size and volume fraction of the precipitates evolve with aging time, and precipitate shape may not be spherical. The kinetics driven evolution of the precipitate size and volume fraction with aging time, and the effects of precipitate shape on the CRSS need to be considered.

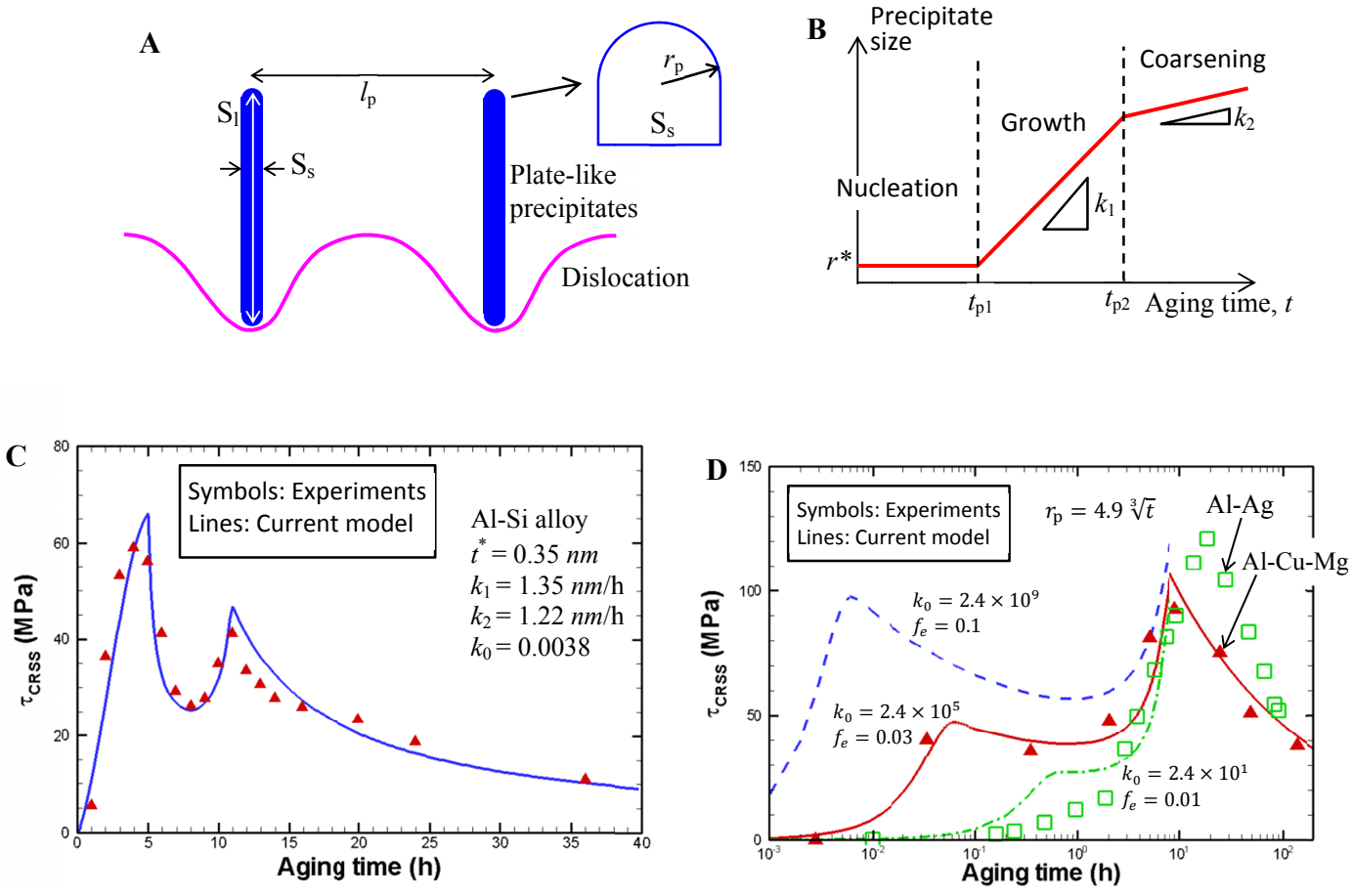

Fig. 4. Comparison between the precipitate shearing model and experiments. (A) Schematic of the interaction between a dislocation and plate-like precipitates. (B) Schematic of the variation of the mean precipitate size with aging time. The latter two figures show a comparison between the age hardening curves predicted by the current model and observed in experiments of (C) Al–Si alloys

with double-peak hardening (Li et al., 2004), (D) Al–Cu–Mg alloys with rapid hardening (Ralston et al., 2010) and Al-Ag alloys with conventional hardening (Lourdjane et al., 2016).

In typical alloys exhibiting double-peak hardening such as Al–Si alloys, the precipitates are in a plate-like shape (Li et al., 2004). Suppose that the precipitates have a large size S_l (length) and a small size S_s (thickness) as illustrated in Fig. 4A, and $S_l = A\ S_s$, where A is the precipitate aspect ratio and equals typically 20. The edges of the precipitate plates may also be regarded as semicircular with radius $r_p = S_s/2$. Therefore, for a given precipitate volume fraction f_p and precipitate size r_p, the precipitate spacing l_p as seen by a traveling dislocation is given by:

$$l_p = r_p \sqrt[3]{\frac{8A^2}{f_p}} = \beta r_p \tag{16}$$

As aforementioned, both f_p and r_p evolve during aging. According to the Johnson-Mehl-Avrami-Kolmogorov model, the precipitate volume fraction f_p grows with the aging time t as

$$\frac{f_p}{f_e} = 1 - \exp(-k_0(\frac{t}{t_0})^4) \tag{17}$$

where f_e is the precipitate volume fraction in the equilibrium state, k_0 is a constant controlling the precipitation rate, and $t_0 = 1\ h$ is a reference time constant. The evolution of the precipitate size r_p is quite complex, which is associated with precipitate nucleation, dissolution, growth and coarsening. In the early aging stage, driven by the supersaturated solid solution, the solute atoms congregate to form precipitates. According to the balance between the interface energy and chemical free energy, a critical nucleation size *r** was identified, below which the precipitates would dissolve and above which they would grow. With increasing aging time, the solute atoms continue to congregate, since the solute concentration is higher than the equilibrium value, leading to precipitate growth. Then, the precipitates stop growing as the solute concentration decreases progressively. Finally, the smaller precipitates shrink, and redeposit onto larger ones, following the Ostwald ripening mechanism (coarsening). Although theoretical analysis suggested that the precipitate size for growth follows $r_p \propto \sqrt{t}$, and the size for coarsening is $r_p \propto \sqrt[3]{t}$, an explicit function of the mean precipitate size evolvement is unavailable because these processes occur simultaneously rather than one after another.

The experimental observations showed that the first hardening peak is a result of GP zones or co-clusters (NiTi) having sizes of ~1 *nm* in the Al–Si based alloys (Li et al., 2004), 2024 aluminum alloys (Zhao et al., 2013), Al–Cu–Mg alloys (Deschamps et al.,

2011) and maraging steels (Pereloma et al., 2004). In the above, we have shown that the CRSS in the early aging stage increases with decreasing precipitate size. Hence, the first CRSS peak must occur at the smallest possible precipitate size, i.e. the critical nucleation radius $r^* \approx 0.5\ nm$. Since the precipitates below r^* dissolve, the stable precipitate radius is always r^* before the first hardening peak at time $t_{p1,}$ as shown in Fig. 4B. After t_{p1}, both precipitate growth and coarsening occur simultaneously. After the second hardening peak at time t_{p2}, only precipitate coarsening occurs. Therefore, we adopt a simple three-segment curve to represent the mean precipitate radius, with rate k_2 being smaller than k_1, as shown in Fig. 4B. The linear relationship was observed as well in experiments (Sankaran and Laird, 1977). In the experiments compared with current model, t_{p1} = 5 h and t_{p2} = 11 h.

With the precipitate size r_p and volume fraction f_p evolving according to Fig. 4B and Eq. (17) respectively, the precipitate spacing l_p calculated from Eq. (16) was used in Eqs. (11) and (12) to calculate the CRSS. A direct comparison between the aging curve predicted by the current model and typically observed in Al–Si alloy experiments (Li et al., 2004) is shown in Fig. 4C. The current model was used to predict the CRSS before t_{p2} (precipitate shearing), while the curve after t_{p2} was predicted from the Orowan model (precipitate bypassing). The current model agrees well with the experimental results, particularly the double-peak hardening. The first peak is induced by the dense nano-precipitates in the early aging stage, while the second one is a result of the transition from dislocations shearing the precipitates to bypassing them. It can be concluded that the first hardening peak is a physical strengthening mechanism, and would have important implications for designing metallic alloys for strength applications. However, in the traditional experiments of aluminum alloys, such as Al–Cu alloys, the double-peak hardening is not obvious. Despite this, a rapid hardening in the early aging stage was commonly observed, resulting in a plateau before the hardening peak (Ashby and Jones, 2013; Ralston et al., 2010). In Fig. 4D, the current model is employed to predict such rapid hardening. Here the precipitate size is predicted by the Lifshitz-Slyozov-Wagner model ($r_\mathrm{p} = 4.9\sqrt[3]{t}$) in the entire aging process. Good agreement is seen between the rapid hardening curves from the current model and experiments. Furthermore, the rapid hardening is eliminated if the precipitation rate is decreased for small values of k_0 and f_e. If the precipitation rate is high for large k_0 and f_e, the rapid hardening changes into the first peak in double-peak hardening. It is seen that the occurrence of the first hardening peak or rapid hardening is controlled by the precipitation rate in the early aging stage.

3.4 A universal law for the conventional hardness peak

Here, we present a further prediction from the precipitate shearing model, which concerns a novel universal law for the second (conventional) hardness peak. As shown in Fig. 2, the influence of the stress decay rate k on the CRSS diminishes as the precipitate size increases. Therefore, when calculating the second hardening peak, the stress decay rate k can be approximated as infinity. As a result, the precipitate size and CRSS at the second hardening peak can be determined by the intersection point between Eqs. (13) and (14):

$$r_{\mathrm{peak2}} = \frac{\beta}{\beta-2}\frac{T}{\gamma} \tag{18}$$

$$\tau_{\mathrm{peak2}} = \frac{2}{\beta}\tau_{\mathrm{in}} = \frac{2\gamma}{\beta b}$$

where β is the precipitate spacing-radius ratio, which equals $\sqrt{\frac{32}{3\pi f_{\mathrm{p}}}}$, $\sqrt[3]{\frac{2\pi A}{f_{\mathrm{p}}}}$, and $\sqrt[3]{\frac{8A^2}{f_{\mathrm{p}}}}$ for sphere, rod and plate shaped precipitates, respectively. Eq. (18) clearly shows that the second hardening peak is mainly dependent on the interface strength τ_{in} or interface energy γ, and the precipitate geometric parameter β. While chemical strengthening was previously claimed to play only a minor role in age hardening (Ardell, 1985), the results here indicate that chemical strengthening strongly influences the second hardening peak. As an important universal trend, the following relation between the second CRSS peak and precipitate radius at which the peak occurs can be obtained from Eqs. (18):

$$\eta\frac{\tau_{\mathrm{peak2}}}{G}\frac{r_{\mathrm{peak2}}}{b} = 1 \tag{19}$$

where $\eta = \beta - 2$. To validate this law, a large number of experimental data on the second CRSS peak and precipitate radius of Al, Fe, Cu and Ni alloys are plotted in a log-log manner in Fig. 5 and listed in Table A1. In Fig. 5, the experimental data mostly fall within a narrow band describable by $\eta\frac{\tau_{\mathrm{peak2}}}{G}\frac{r_{\mathrm{peak2}}}{b} \approx C$, which is in good agreement with Eq. (19). However, the fitting constant C is 0.34±0.024 and lower than the unity in Eq. (19). This is not unreasonable since the interface strength is constant for all precipitates in the current model, while it may increase by several times for incoherent, large precipitates. Therefore, the transition from precipitate shearing to bypassing would occur earlier during experimental aging process, leading to lower peak stress and precipitate radius. In addition, the current model is derived from one dislocation passing through an orderly precipitate field, while in experiments, precipitates have a random distribution and result in a weaker hardening effect. Therefore, Eq. (19) should be the upper limit of

the CRSS peak and precipitate size, as demonstrated clearly by Fig. 5. To the best of our knowledge, this is the first analytical model to predict the maximum strengthening effects achieved by aging or precipitation, which is of general significance for the design of metallic alloys for strength applications.

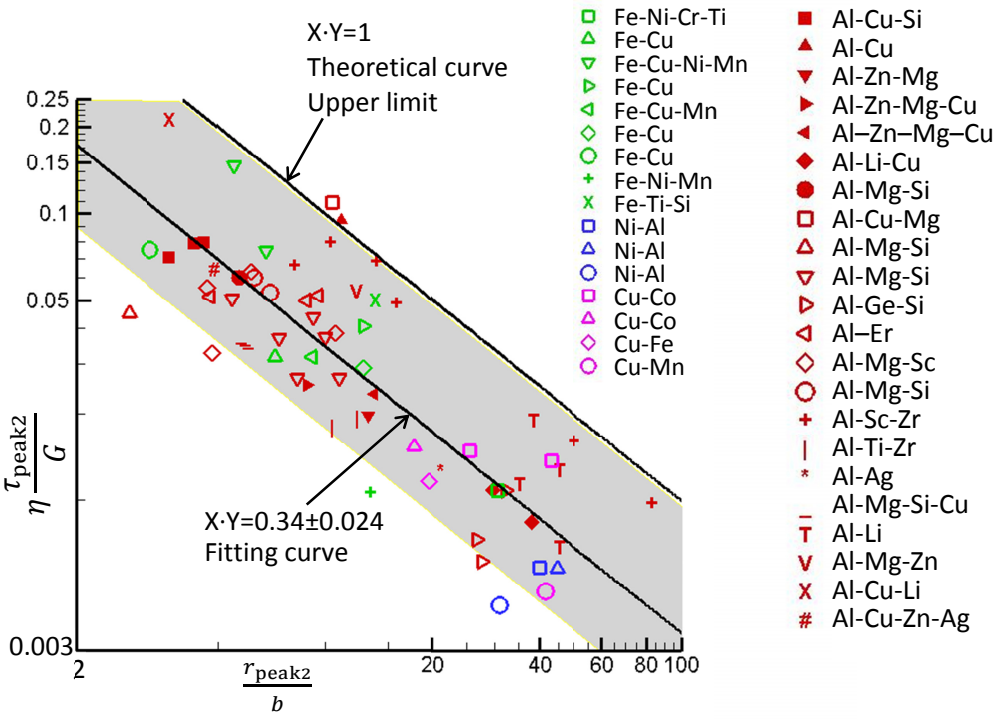

Fig. 5. The relationship between the second CRSS peak and precipitate radius. References and data of this figure are listed in Table A1 in Appendix A.

Since the coherency strengthening effect dominates for small precipitates in the early aging stage, the first CRSS peak can also be predicted from Eq. (15):

$$r_{\text{peak1}} = r^* \tag{20}$$

$$\tau_{\text{peak1}} = 2\frac{\sqrt{2t^*r^*+t^{*2}}}{l_{\text{p}}}\tau_{\text{in}} = \sqrt{\frac{3\pi f_{\text{p}}}{8}}\sqrt{(\frac{t^*}{r^*})^2+2\frac{t^*}{r^*}}\tau_{\text{in}}$$

It can be seen that the first CRSS peak is related to the effective stress zone thickness t^* and the volume fraction f_{p} of the precipitates. Therefore, the double-peak hardening occurs favorably for those alloys having large coherency strain and rapid precipitation. Assuming $t^* \approx r^*$, we can obtain the following relationship between the two CRSS peaks

$$\frac{\tau_{\text{peak1}}}{\tau_{\text{peak2}}} = \sqrt{3\frac{f_{\text{peak1}}}{f_{\text{peak2}}}} \tag{21}$$

The first CRSS peak, τ_{peak1}, exceeds the second peak, τ_{peak2}, at volume fraction $f_{\text{peak1}} > 0.33\, f_{\text{peak2}}$, indicating that in order to observe the first hardening peak, rapid precipitation

in the early aging stage is required. This was already proven in the Al-Si alloy experiments (Li et al., 2004), where the first hardening peak becomes remarkable at high temperatures as a result of high precipitation rate. Since the first hardening peak provides a new approach to strengthen materials, future efforts could be made towards accelerating the precipitation in the early aging stage and adding those alloying elements that would induce a large coherency strain. As shown in Ref. (Runxia et al., 2010), the addition of Cd/Sn in the Al-Si alloys was observed to accelerate the precipitation in the early aging stage and, as a result, the aging curves showed enhanced first hardness peak and negligible second one.

4. Summary and conclusions

In this work, molecular dynamics simulations were firstly conducted to reveal a coarse-grained force law between dislocations and precipitates, which was then introduced into discrete dislocation dynamics method to study the interaction between a dislocation and an array of spherical precipitates at multi-scales. The discrete dislocation dynamics simulations showed that the critical resolved shear stress (CRSS) for a dislocation passing through a precipitate field with a constant volume fraction can be divided into three regimes. The first regime is a decrease with increasing precipitate radius, as a result of the coherency strengthening mechanism ($\tau_{\mathrm{coh}} \propto r_{\mathrm{p}}^{-1/2}$ in Eq. 15), while the second regime is an increase associated with chemical strengthening ($\tau_{\mathrm{chem}} \propto -r_{\mathrm{p}}^{-1}$ in Eq. 14). These two regimes are governed intricately by the precipitate-matrix interface strength, the stress zones around the precipitates and their spacing, and the local curvature of the interacting dislocation. The decrease of CRSS in the third regime is attributed to the conventional Orowan mechanism ($\tau_{\mathrm{Orowan}} \propto r_{\mathrm{p}}^{-1}$ in Eq. 13). Then, a precipitate shearing model (Eq. 12) was proposed, and found to agree well with the discrete dislocation dynamics results. From the current simulations and precipitate shearing model, it is shown that alloy materials are significantly hardened by nano-precipitates in the early aging stage. As a result, the first hardening peak is a physical strengthening mechanism, in addition to the second hardening peak observed conventionally. By introducing variations of the precipitate size and volume fraction with aging time, the aging curve with double CRSS peaks predicted by the current model agrees well with that observed in experiments. In addition, even though double-peak CRSS is not always observed in experiments, rapid hardening is commonly observed in the early aging stage, and the current model is able to

predict such rapid hardening as well. Finally, based on the current precipitate shearing model, analytical expressions of the two CRSS peaks were deduced. The second CRSS peak was found to follow an inverse relationship with the precipitate size at peak strength, and this trend is in good agreement with experimental data from a large pool of studies. By comparing the two CRSS peaks, the first CRSS peak is found to occur favorably for those materials with large coherency strain and rapid precipitation in the early aging stage. Since the first hardening peak provides a new approach to strengthen materials, future efforts could be made towards accelerating the precipitation in the early aging stage and adding alloying elements that could induce large coherency strain.

Acknowledgments

The financial support from the National Natural Science Foundation of China (U1730106, 11672193) is acknowledged. AHWN acknowledges support from the endowment fund of Kingboard Professorship in Materials Engineering. JAE acknowledges support by the National Science Foundation CAREER Award #CMMI-1454072.

Appendix A

Table A1. Experimental data of Al, Fe, Cu and Ni alloys. All the data are used in Fig. 5.

Material	Precipitate shape	Large size (nm)	Small size (nm)	CRSS (MPa)	Volume fraction	η
Al-Cu-Si (Weakley-Bollin et al., 2004)	plate	53.18	2.45	74.69	0.15	27.29
		77.85	2.62	60.42	0.15	34.11
		79.19	2.09	45.25	0.15	40.53
Al-Cu (Tsuji et al., 2004)	plate	479.47	6.37	23.80	0.038	103.67
Al-Zn-Mg (Deschamps et al., 1999)	sphere	7.56	7.56	65.24	0.035	7.87
Al-Zn-Mg-Cu (Deschamps et al., 1999)	sphere	5.12	5.12	95.72	0.043	6.88
Al–Zn–Mg–Cu (Fribourg et al., 2011)	sphere	7.88	7.88	111.5	0.061	5.48
Al-Li-Cu (Huang and Ardell, 1988)	sphere	21.74	21.74	42.30	0.066	5.15
		16.87	16.87	40.89	0.043	6.91
Al-Mg-Si (Myhr et al., 2001)	rod	65.65	3.28	78.08	0.0118	20.01
Al-Cu-Mg (Liu et al.,	plate	179.78	6.0	48.18	0.032	58.75

2003)						
Al-Mg-Si (Liu et al., 2003)	rod	54.46	1.61	54.12	0.016	21.69
Al-Mg-Si (Småbråten, 2011)	rod	86.04	4.78	30.27	0.0072	23.04
		42.56	3.14	60.8	0.0064	21.70
		44.39	4.25	46.3	0.0056	20.71
		71.75	5.73	40.87	0.0047	23.58
		67.14	5.32	57.37	0.0078	19.66
		87.6	6.25	32.63	0.007	21.25
Al-Ge-Si (Gan, 2006)	sphere	18.4	18.4	19.46	0.0124	14.55
		15.7	15.7	10.85	0.0122	14.69
		15.2	15.2	12.5	0.0114	15.26
Al–Er (Zhang et al., 2014)	sphere	5.48	5.48	29.53	0.0015	45.59
		5.09	5.09	28.48	0.0015	45.59
		2.71	2.71	29.27	0.0015	45.59
Al-Mg-Sc (Marquis, 2002)	sphere	2.76	2.76	42.58	0.007	20.03
		6.12	6.12	49.6	0.007	20.03
		2.67	2.67	71.65	0.007	20.03
		3.53	3.53	81.44	0.007	20.03
Al-Mg-Si (Cuniberti et al., 2010)	rod	17.6	4	114.84	0.01	12.03
		29	3.6	102.64	0.01	15.17
Al-Sc-Zr (Fuller, 2003)	sphere	5.94	5.94	61.54	0.0027	33.47
		4.7	4.7	84.8	0.0069	20.19
		28.8	28.8	13	0.0029	32.22
		8	8	86	0.0066	20.69
		47.5	47.5	7.9	0.0029	32.22
		9.06	9.06	62	0.0067	20.52
Al-Ti-Zr (Tsau and Chen, 2002)	sphere	7.07	7.07	80.83	0.05	6.24
		6	6	75.45	0.05	6.24
Al-Ag (Gerold and Hartmann, 1968)	sphere	12.12	12.12	28	0.018	11.74
Al-Mg-Si-Cu (Esmaeili et al., 2003)	rod	68.03	3.4	40.8	0.0072	23.93
		66.45	3.3	41.5	0.0072	23.93
		69.50	3.47	39.7	0.0072	23.93
Al-Li (Noble et al., 1982)	sphere	26	26	12.23	0.004	27.14
		22	22	71.83	0.043	6.89
		20	20	93.98	0.128	3.15
		26	26	92.46	0.22	1.93
Al-Mg-Zn (Melander and Persson, 1978)	sphere	7	7	94.1	0.012	14.83
A1-Cu-Li (Nie and Muddle, 1998)	plate	135.04	2.09	30.49	0.0055	180.3
Al-Cu-Zn-Ag (Scott et al., 1987)	plate	31.48	2.79	70.0	0.06	23.71
Fe-Ni-Cr-Ti (Thompson and	sphere	15.27	15.27	223.5	0.095	3.98

Brooks, 1982)						
Fe-Cu (Youle and Ralph, 1972)	sphere	3.6	3.6	183.27	0.013	14.17
Fe-Cu-Ni-Mn (Osamura et al., 1994)	sphere	3.41	3.41	145.19	0.0018	42.07
		2.77	2.77	133.1	0.0004	90.16
Fe-Cu (Deschamps et al., 2003)	sphere	6.4	6.4	105	0.003	31.65
Fe-Cu-Mn (Deschamps et al., 2003)	sphere	4.6	4.6	85	0.0032	30.58
Fe-Cu (Deschamps et al., 2001)	sphere	6.4	6.4	92.5	0.0044	25.79
Fe-Cu (Holzer and Kozeschnik, 2010)	sphere	1.61	1.61	162.45	0.0022	37.74
Fe-Ni-Mn (Pereloma et al., 2004)	plate	16.5	6.7	184.67	0.16	4.716
Fe-Ti-Si (Jack and Honeycombe, 1972)	sphere	6.92	6.92	454.38	0.028	9.01
Ni-Al (Shimanuki and Doi, 1974)	sphere	20	20	267.58	0.245	1.72
Ni-Al (Ardell, 1985)	sphere	22.46	22.46	92.2	0.07	4.97
Ni-Al (Phillips, 1966)	sphere	15.41	15.41	184.57	0.23	1.84
Cu-Co (Amin et al., 1975)	sphere	13	13	56.9	0.016	12.57
		22	22	45.6	0.0124	14.55
Cu-Co (Phillips, 1965)	sphere	9.8	9.8	76.62	0.025	9.66
Cu-Fe (Matsuura et al., 1978)	sphere	10	10	37.87	0.012	14.83
Cu-Mn (Yeomans and McCormick, 1978)	sphere	21.22	21.22	49.06	0.075	4.73

References

Aaronson, H., 1974. Observations on interphase boundary structure. J Microsc. 102, 275-300.

Amin, K.E., Gerold, V., Kralik, G., 1975. The plastic deformation of copper-2 at.% cobalt alloy single crystals. J. Mater. Sci. 10, 1519-1526.

Ardell, A., 1985. Precipitation hardening. Metall. Trans. A 16, 2131-2165.

Argon, A., 2007. Strengthening Mechanisms in Crystal Plasticity. Oxford University Press.

Arsenlis, A., Cai, W., Tang, M., Rhee, M., Oppelstrup, T., Hommes, G., Pierce, T.G., Bulatov, V.V., 2007. Enabling strain hardening simulations with dislocation dynamics. Model. Simul. Mater. Sci. Eng. 15, 553-595.

Ashby, M.F., Jones, D.R.H., 2013. Chapter 11 - Light Alloys. Butterworth-Heinemann, Boston.

Askari, H., Zbib, H.M., Sun, X., 2013. Multiscale Modeling of Inclusions and Precipitation Hardening in Metal Matrix Composites: Application to Advanced High-Strength Steels. J. Nanomech. Micromech. 3, 24-33.

Benzerga, A.A., Bréchet, Y., Needleman, A., Giessen, E.V.d., 2004. Incorporating three-dimensional mechanisms into two-dimensional dislocation dynamics. Model. Simul. Mater. Sci. Eng. 12, 159.

Cook, J.D., Nutting, J., 1969. Effect of Plastic Deformation on the θ''→θ'Transformation during the Ageing of an Al - 4% Cu Alloy at 160 ℃. The Institute of Metals, London.

Cuniberti, A., Tolley, A., Riglos, M.V.C., Giovachini, R., 2010. Influence of natural aging on the precipitation hardening of an AlMgSi alloy. Mater. Sci. Eng. A 527, 5307-5311.

Deschamps, A., Bastow, T.J., de Geuser, F., Hill, A.J., Hutchinson, C.R., 2011. In situ evaluation of the microstructure evolution during rapid hardening of an Al–2.5Cu–1.5Mg (wt.%) alloy. Acta Mater. 59, 2918-2927.

Deschamps, A., Bréchet, Y., Livet, F., 1999. Influence of copper addition on precipitation kinetics and hardening in Al–Zn–Mg alloy. Mater. Sci. Tech 15, 993-1000.

Deschamps, A., Militzer, M., Poole, W., 2001. Precipitation kinetics and strengthening of a Fe–0.8 wt% Cu alloy. ISIJ Int. 41, 196-205.

Deschamps, A., Militzer, M., Poole, W., 2003. Comparison of precipitation kinetics and strengthening in an Fe-0.8% Cu alloy and a 0.8% Cu-containing low-carbon steel. ISIJ Int. 43, 1826-1832.

El-Awady, J.A., 2015. Unravelling the physics of size-dependent dislocation-mediated plasticity. Nat. Commun. 6.

Esmaeili, S., Lloyd, D.J., Poole, W.J., 2003. A yield strength model for the Al-Mg-Si-Cu alloy AA6111. Acta Mater. 51, 2243-2257.

Fan, H., Aubry, S., Arsenlis, A., El-Awady, J.A., 2015a. Orientation influence on grain size effects in ultrafine-grained magnesium. Scripta Mater. 97, 25-28.

Fan, H., Aubry, S., Arsenlis, A., El-Awady, J.A., 2015b. The role of twinning deformation on the hardening response of polycrystalline magnesium from discrete dislocation dynamics simulations. Acta Mater. 92, 126-139.

Fan, H., Aubry, S., Arsenlis, A., El-Awady, J.A., 2016. Grain size effects on dislocation and twinning mediated plasticity in magnesium. Scripta Mater. 112, 50-53.

Fan, H., El-Awady, J.A., Wang, Q., 2015c. Towards further understanding of stacking fault tetrahedron absorption and defect-free channels – A molecular dynamics study. J. Nucl. Mater. 458, 176-186.

Fan, H., Li, Z., Huang, M., Zhang, X., 2011. Thickness effects in polycrystalline thin films: Surface constraint versus interior constraint. Int. J. Solids Struct. 48, 1754-1766.

Fan, H., Wang, Q., Tian, X., El-Awady, J.A., 2017. Temperature effects on the mobility of pyramidal <c + a> dislocations in magnesium. Scripta Mater. 127, 68-71.

Fan, H., Zhu, Y., El-Awady, J.A., Raabe, D., 2018. Precipitation hardening effects on extension twinning in magnesium alloys. Int. J. Plast. 106, 186-202.

Fribourg, G., Bréchet, Y., Deschamps, A., Simar, A., 2011. Microstructure-based modelling of isotropic and kinematic strain hardening in a precipitation-hardened aluminium alloy. Acta Mater. 59, 3621-3635.

Fuller, C.B., 2003. Temporal evolution of the microstructures of Al (Sc, Zr) alloys and their influences on mechanical properties. PHD thesis.

Gan, W., 2006. Precipitation and strengthening in AL-GE-SI alloys. PHD thesis.

Gao, Y., Zhuang, Z., Liu, Z.L., You, X.C., Zhao, X.C., Zhang, Z.H., 2011. Investigations of pipe-diffusion-based dislocation climb by discrete dislocation dynamics. Int. J. Plast. 27, 1055-1071.

Gerold, V., Hartmann, K., 1968. Theoretical and experimental investigations on stacking fault strengthening, Trans. Jpn. Inst. Met. . JAPAN INST METALS AOBA ARAMAKI, SENDAI 980, JAPAN, pp. 509-&.

Ghoniem, N.M., Tong, S.H., Sun, L.Z., 2000. Parametric dislocation dynamics: A thermodynamics-based approach to investigations of mesoscopic plastic deformation. Phys. Rev. B 61, 913-927.

He, J.Y., Wang, H., Huang, H.L., Xu, X.D., Chen, M.W., Wu, Y., Liu, X.J., Nieh, T.G., An, K., Lu, Z.P., 2016. A precipitation-hardened high-entropy alloy with outstanding tensile properties. Acta Mater. 102, 187-196.

Hirth, J.P., Lothe, J., 1982. Theory of Dislocations, 2nd ed. John Wiley and Sons, New York.

Holzer, I., Kozeschnik, E., 2010. Computer simulation of the yield strength evolution in Cu-precipitation strengthened ferritic steel. Mater. Sci. Eng. A 527, 3546-3551.

Hou, C., Li, Z., Huang, M., Ouyang, C., 2008. Discrete dislocation plasticity analysis of single crystalline thin beam under combined cyclic tension and bending. Acta Mater. 56, 1435-1446.

Huang, J.C., Ardell, A.J., 1988. Addition rules and the contribution of δ' precipitates to strengthening of aged Al Li Cu alloys. Acta Metall. 36, 2995-3006.

Huang, M., Tong, J., Li, Z., 2014. A study of fatigue crack tip characteristics using discrete dislocation dynamics. Int. J. Plast. 54, 229-246.

Huang, M., Zhao, L., Tong, J., 2012. Discrete dislocation dynamics modelling of mechanical deformation of nickel-based single crystal superalloys. Int. J. Plast. 28, 141-158.

Hussein, A.M., Rao, S.I., Uchic, M.D., Dimiduk, D.M., El-Awady, J.A., 2015. Microstructurally based cross-slip mechanisms and their effects on dislocation microstructure evolution in fcc crystals. Acta Mater. 85, 180-190.

Hutchinson, C.R., Nie, J.F., Gorsse, S., 2005. Modeling the precipitation processes and strengthening mechanisms in a Mg-Al-(Zn) AZ91 alloy. Metall. Mater. Trans. A 36, 2093-2105.

Jack, D., Honeycombe, R., 1972. Age hardening of an Fe-Ti-Si alloy. Acta Metall. 20, 787-796.

Kaçar, R., Güleryüz, K., 2015. Effect of Quenching Rate and Pre-strain on the Strain Ageing Behaviors of 7075 Aluminum Alloys. Mater. Res. 18, 328-333.

Kubin, L.P., Canova, G., Condat, M., Devincre, B., Pontikis, V., Brechet, Y., 1992. Dislocation microstructures and plastic flow: A 3D simulation. Solid State Phenom. 23 & 24, 455-472.

Lehtinen, A., Granberg, F., Laurson, L., Nordlund, K., Alava, M.J., 2016. Multiscale modeling of dislocation-precipitate interactions in Fe: From molecular dynamics to discrete dislocations. Phys. Rev. E 93, 013309.

Li, R.X., Li, R.D., Zhao, Y.H., He, L.Z., Li, C.X., Guan, H.R., Hu, Z.Q., 2004. Age-hardening behavior of cast Al–Si base alloy. Mater. Lett. 58, 2096-2101.

Liu, F.X., Liu, Z.L., Pei, X.Y., Hu, J.Q., Zhuang, Z., 2017. Modeling high temperature anneal hardening in Au submicron pillar by developing coupled dislocation glide-climb model. Int. J. Plast. 99, 102-119.

Liu, G., Zhang, G.J., Ding, X.D., Sun, J., Chen, K.H., 2003. Modeling the strengthening response to aging process of heat-treatable aluminum alloys containing plate/disc- or rod/needle-shaped precipitates. Mater. Sci. Eng. A 344, 113-124.

Liu, X.Y., Adams, J.B., 1998. Grain-boundary segregation in Al–10%Mg alloys at hot working temperatures. Acta Mater. 46, 3467-3476.

Liu, Z.L., Liu, X.M., Zhuang, Z., You, X.C., 2009. A multi-scale computational model of crystal plasticity at submicron-to-nanometer scales. Int. J. Plast. 25, 1436-1455.

Lourdjane, F., Kadi-Hanifi, M., Raho, A.A., 2016. Precipitation of the metastable phases in a tin microalloyed Al-10at% Ag alloy. AIMS Mater. Sci. 4, 1.

Luo, A.A., 2013. Magnesium casting technology for structural applications. J. Magn. Alloy. 1, 2-22.

Marquis, E.A., 2002. Microstructural evolution and strengthening mechanisms in Al-Sc and Al-Mg-Sc alloys. PHD thesis.

Matsuura, K., Kitamura, M., Watanabe, K., 1978. The Precipitation Hardening of Cu–Fe Alloy Single Crystals with Coherent γ-Iron Particles. Trans. Jpn. Inst. Met. 19, 53-59.

Melander, A., Persson, P.Å., 1978. The strength of a precipitation hardened AlZnMg alloy. Acta Metall. 26, 267-278.

Mimica, R., 2015. HARDNESS VERSUS TIME DEPENDENCY DURING ARTIFICIAL AGEING OF AlMgSi0. 5 ALUMINIUM ALLOY. Zbornik Sveučilišta u Dubrovniku 2, 261-270.

Myhr, O.R., Grong, Ø., Andersen, S.J., 2001. Modelling of the age hardening behaviour of Al–Mg–Si alloys. Acta Mater. 49, 65-75.

Nicholson, R.B., Nutting, J., 1961. The metallography of precipitation in an Al-16% Ag alloy. Acta Metall. 9, 332-343.

Nie, J.F., Muddle, B.C., 1998. Microstructural design of high-strength aluminum alloys. J. Phase Equilib. 19, 543.

Noble, B., Harris, S.J., Dinsdale, K., 1982. Yield characteristics of aluminium–lithium alloys. Metal Sci. 16, 425-430.

Osamura, K., Okuda, H., Ochiai, S., Takashima, M., Asano, K., Furusaka, M., Kishida, K., Kurosawa, F., 1994. Precipitation hardening in Fe-Cu binary and quaternary alloys. ISIJ Int. 34, 359-365.

Pereloma, E.V., Shekhter, A., Miller, M.K., Ringer, S.P., 2004. Ageing behaviour of an Fe–20Ni–1.8Mn–1.6Ti–0.59Al (wt%) maraging alloy: clustering, precipitation and hardening. Acta Mater. 52, 5589-5602.

Phillips, V., 1966. A metallographic study of precipitation in a ni-12.7 at.% al alloy. Acta Metall. 14, 1533-1547.

Phillips, V.A., 1965. Effect of coherency strain fields on the flow stress of a copper-3·12% cobalt alloy. Philos. Mag. 11, 775-797.

Plimpton, S., 1995. Fast Parallel Algorithms for Short-Range Molecular Dynamics. J. Comput. Phys. 117, 1-19.

Purja Pun, G.P., Mishin, Y., 2009. Development of an interatomic potential for the Ni-Al system. Philos. Mag. 89, 3245-3267.

Ralston, K.D., Birbilis, N., Weyland, M., Hutchinson, C.R., 2010. The effect of precipitate size on the yield strength-pitting corrosion correlation in Al–Cu–Mg alloys. Acta Mater. 58, 5941-5948.

Runxia, L., Yujin, C., Xiaoguang, Y., Yingdong, Q., Rongde, L., 2010. Effects of Cd and Sn on double-peak age-hardening behaviors of Al-Si-Cu-Mg cast alloys. Research & Development.

Sankaran, R., Laird, C., 1977. On the Kinetics of growth of plate precipitates in Al-Ag, Al-Au and Al-Cu alloys. Scripta Metall. 11, 383-386.

Scott, V.D., Kerry, S., Trumper, R.L., 1987. Nucleation and growth of precipitates in Al–Cu–Mg–Ag alloys. Mater. Sci. Tech 3, 827-835.

Shekhter, A., Aaronson, H.I., Miller, M.R., Ringer, S.P., Pereloma, E.V., 2004. Effect of aging and deformation on the microstructure and properties of Fe-Ni-Ti maraging steel. Metall. Mater. Trans. A 35, 973-983.

Shimanuki, Y., Doi, H., 1974. Effect of Aging Treatment on Microstructure and Tensile Properties of Udimet 520 and Ni-6.38%Al Alloy. Trans. Jpn. Inst. Met. 15, 24-31.

Shin, C.S., Fivel, M.C., Verdier, M., Oh, K.H., 2003. Dislocation–impenetrable precipitate interaction: a three-dimensional discrete dislocation dynamics analysis. Philos. Mag. 83, 3691-3704.

Silva, E.P.d., Batista, L.F., Callegari, B., Buzolin, R.H., Warchomicka, F., Requena, G.C., Brito, P.P., Pinto, H.C., 2014. Solution and ageing heat treatments of ZK60 magnesium alloys with rare earth additions produced by semi-solid casting. Mater. Res. 17, 1507-1512.

Singh, A.K., Louat, N., Sadananda, K., 1988. Dislocation network formation and coherency loss around gamma- prime precipitates in a nickel- base superalloy. Metall. Trans. A 19, 2965-2973.

Småbråten, H.K., 2011. Characterization of precipitates at maximum hardness and overaged conditions in Al-Mg-Si alloys. Master thesis.

Starink, M.J., Wang, S.C., 2009. The thermodynamics of and strengthening due to co-clusters: General theory and application to the case of Al–Cu–Mg alloys. Acta Mater. 57, 2376-2389.

Takahashi, A., Ghoniem, N.M., 2008. A computational method for dislocation–precipitate interaction. J. Mech. Phys. Solids 56, 1534-1553.

Tan, C.F., Said, M.R., 2009. Effect of hardness test on precipitation hardening aluminium alloy 6061-T6. Chiang Mai J. Sci 36, 276-286.

Thompson, A.W., Brooks, J.A., 1982. The mechanism of precipitation strengthening in an iron-base superalloy. Acta Metall. 30, 2197-2203.

Tsau, C.-H., Chen, Y.-C., 2002. The coarsening of the precipitates in melt-spun Al–Ti–Zr ribbons. Mater. Chem. Phys. 73, 111-117.

Tsuji, N., Iwata, T., Sato, M., Fujimoto, S., Minamino, Y., 2004. Aging behavior of ultrafine grained Al–2 wt%Cu alloy severely deformed by accumulative roll bonding. Sci. Technol. Adv. Mat. 5, 173-180.

Van der Giessen, E., Needleman, A., 1995. Discrete dislocation plasticity: a simple planar model Model. Simul. Mater. Sci. Eng. 3, 689-735.

Weakley-Bollin, S.C., Donlon, W., Wolverton, C., Allison, J.E., Jones, J.W., 2004. Modeling the age-hardening behavior of Al-Si-Cu alloys. Metall. Mater. Trans. A 35, 2407-2418.

Wilm, A., 1911. The hardening of light alimiinum alloys. Metallurgie 8, 225.

Xu, W., Rivera-Díaz-del-Castillo, P.E.J., Wang, W., Yang, K., Bliznuk, V., Kestens, L.A.I., van der Zwaag, S., 2010a. Genetic design and characterization of novel ultra-high-strength stainless steels strengthened by Ni3Ti intermetallic nanoprecipitates. Acta Mater. 58, 3582-3593.

Xu, W., Rivera-Díaz-del-Castillo, P.E.J., Yan, W., Yang, K., San Martín, D., Kestens, L.A.I., van der Zwaag, S., 2010b. A new ultrahigh-strength stainless steel strengthened by various coexisting nanoprecipitates. Acta Mater. 58, 4067-4075.

Yang, X., Liu, J., Chen, J., Wan, C., Fang, L., Liu, P., Wu, C., 2014. Relationship Between the Strengthening Effect and the Morphology of Precipitates in Al–7.4 Zn–1.7 Mg–2.0 Cu Alloy. Acta Metall. Sin. (Engl. Lett.) 27, 1070-1077.

Yeomans, S., McCormick, P., 1978. An investigation of precipitation and strengthening in age-hardening copper-manganese alloys. Mater. Sci. Eng. 34, 101-109.

Youle, A., Ralph, B., 1972. A Study of the Precipitation of Copper from α-Iron in the Pre-Peak to Peak Hardness Range of Ageing. Metal Sci. J. 6, 149-152.

Záležák, T., Svoboda, J., Dlouhý, A., 2017. High temperature dislocation processes in precipitation hardened crystals investigated by a 3D discrete dislocation dynamics. Int. J. Plast. 97, 1-23.

Zbib, H.M., Diaz de la Rubia, T., 2002. A multiscale model of plasticity. Int. J. Plast. 18, 1133-1163.

Zhang, Y., Gao, K., Wen, S., Huang, H., Nie, Z., Zhou, D., 2014. The study on the coarsening process and precipitation strengthening of Al3Er precipitate in Al–Er binary alloy. J. Alloy. Compd. 610, 27-34.

Zhang, Y., Ngan, A.H.W., 2018. Dislocation-density dynamics for modeling the cores and Peierls stress of curved dislocations. Int. J. Plast. 104, 1-22.

Zhao, Y.L., Yang, Z.Q., Zhang, Z., Su, G.Y., Ma, X.L., 2013. Double-peak age strengthening of cold-worked 2024 aluminum alloy. Acta Mater. 61, 1624-1638.

Zhou, X.W., Johnson, R.A., Wadley, H.N.G., 2004. Misfit-energy-increasing dislocations in vapor-deposited CoFe/NiFe multilayers. Phys. Rev. B 69, 144113.

Zhu, Y., Li, Z., Huang, M., 2013. Atomistic modeling of the interaction between matrix dislocation and interfacial misfit dislocation networks in Ni-based single crystal superalloy. Comput. Mater. Sci. 70, 178-186.